

Edge detection of potential field anomalies using the Gompertz function as a high-resolution edge enhancement filter

A. ALVANDI AND V.E. ARDESTANI

Institute of Geophysics, University of Tehran, Tehran, Iran

(Received: 7 January 2023; accepted: 3 April 2023; published online: 8 June 2023)

ABSTRACT Localising horizontal boundaries and edge enhancement is an essential process in interpreting magnetic and gravity data. Standard edge enhancement filters have the disadvantage of producing false horizontal boundaries with low-resolution maps. The goal of the present work is to visualise source boundaries by eliminating false edges, so as to obtain high-resolution results. The study presents a high-resolution edge delineation filter based on the Gompertz function (*GF*) and an improved horizontal derivative to enhance potential field data. The new balanced filter was first tested on synthetic data from prismatic model sources and Bishop synthetic models. The filter was, then, applied to the aeromagnetic data set from the state of Georgia (U.S.A.) and gravity field data from the Gol-e-Gohar iron ore mine in Kerman Province (Iran). The accuracy of the filter was evaluated by comparing the results obtained with those of other standard filters. The obtained results show that the *GF* high-resolution filter is capable of simultaneously determining the lateral boundaries of buried structures with different depths. Therefore, the *GF* filter can be considered reliable when used for qualitative interpretation of gravity and magnetic data.

Key words: total horizontal derivative, edge detection, Gompertz function, potential field data.

1. Introduction

Edge enhancement filters for potential field anomalies play a critical role in interpreting geologic features such as faults, dikes, and contacts, and in mapping structural lineaments in the subsurface (Cooper and Cowan, 2006; Sun *et al.*, 2016; Dwivedi and Chamoli, 2021; Pham *et al.*, 2021; Alvandi *et al.*, 2022b; Prasad *et al.*, 2022). In recent years, several edge enhancement filters have been introduced and developed for the lateral localisation of subsurface magnetic and gravity anomalies (Chen *et al.*, 2017; Nasuti and Nasuti, 2018; Weihermann *et al.*, 2018). These filters distinguish points in filtered images where physical features change or are significantly discontinuous (Eldosouky, 2019). These filters are often introduced and developed on the basis of the directional derivatives of potential field data. Some of the edge detection filters are not able to accurately determine the horizontal boundaries of the buried sources, or the output images are not of good resolution. Therefore, the improvement of the quality and accuracy of edge detection filters play an important role in the accurate interpretation of potential field data.

2. Standard edge detection filters

The total horizontal derivative (*THDR*) filter, introduced by Cordell and Grauch (1985), is one of the most commonly used filters. The amplitude maxima are positioned over the edge of the causative source frames; for this reason, this type of filter can be used to detect horizontal lateral boundaries. However, the *THDR* filter cannot equalise the edges of bodies with different depths and superimposed geological structures (Fedi and Florio, 2001; Prasad *et al.*, 2022). The *THDR* filter is defined as:

$$THDR = \sqrt{\left(\frac{\partial T}{\partial x}\right)^2 + \left(\frac{\partial T}{\partial y}\right)^2}. \quad (1)$$

In Eq. 1, T is the gravity or magnetic data which is reduced to pole (RTP), and $\left(\frac{\partial T}{\partial x}\right)$ and $\left(\frac{\partial T}{\partial y}\right)$ are the first-order horizontal gradients of potential field data (Cooper and Cowan, 2006).

The analytical signal amplitude (*ASA*) or total gradient filter, is another linear edge delineation filter introduced by Roest *et al.* (1992). The amplitude maxima are directed over the edge centre and can, therefore, be used to delineate the horizontal location of geological structures. Like the *THDR* filter, the *ASA* filter cannot balance the edges of various body sources and superimposed anomalies, and cannot distinguish the lateral boundaries of thin sources (Oksum *et al.*, 2021; Prasad *et al.*, 2022). The *ASA* filter is defined as:

$$ASA = \sqrt{\left(\frac{\partial T}{\partial x}\right)^2 + \left(\frac{\partial T}{\partial y}\right)^2 + \left(\frac{\partial T}{\partial z}\right)^2}. \quad (2)$$

In Eq. 2, $\left(\frac{\partial T}{\partial z}\right)$ is the vertical gradient of the potential field data and $\left(\frac{\partial T}{\partial x}\right)$ and $\left(\frac{\partial T}{\partial y}\right)$ are defined in Eq. 1. Therefore, the *THDR* and *ASA* filters can only determine the horizontal lateral boundaries of the sources with strong amplitudes due to the fact that the edges of the sources at deeper depths have low resolutions (Pham *et al.*, 2019; Prasad *et al.*, 2022). To solve this problem and determine the lateral boundaries of different anomalies, at different depths and with simultaneously-effective small and large amplitudes, phase-based algorithms or local phase filters have been introduced and developed. Essentially, these filters (local phase) have been obtained by normalising the *THDR*, *ASA*, etc. filters (Alvandi *et al.*, 2022c).

The first filter applied the tilt angle (*TA*) method by Miller and Singh (1994). Such method consists in using the vertical gradient and magnitude of the total horizontal gradient of the potential field data. The *TA* method applies zero crossing to delineate the edges and horizontal boundaries and is much easier to interpret compared to the *THDR* and *ASA* filters (Cooper and Cowan, 2006). The *TA* method is defined as:

$$TA = \tan^{-1} \left(\frac{\frac{\partial T}{\partial z}}{THDR} \right). \quad (3)$$

However, the horizontal boundaries of sources with different wavelengths are determined simultaneously, but *TA* is usually unable to clearly identify the edges, therefore, proving an unsuccessful method for thin and deep structures (Prasad *et al.*, 2022).

Wijns *et al.* (2005) introduced another filter, the theta map (*TM*) filter. This filter uses the *ASA* to normalise the *THDR* method. The *TM* filter is defined as:

$$TM = \cos^{-1} \left(\frac{THDR}{ASA} \right). \quad (4)$$

Although this filter minimum is directed over the lateral boundaries of the causative sources, it produces false and spurious edges, and is less effective in edge detection of thin and deep-lying sources (Alvandi *et al.*, 2022c; Prasad *et al.*, 2022). In addition, the enhanced lateral boundaries appear more diffused and wider than in reality (Nasuti *et al.*, 2019).

Cooper and Cowan (2006) proposed a modified version of the tilt angle: the horizontal tilt angle (*TDX*). The *TDX* approach applies the absolute value of the vertical gradient to normalise the *THDR* amplitude. Results obtained are similar to those obtained with the *TM* filter, and secondary edges in the filtered images are produced, even though the maximum filter values are used to determine the horizontal boundaries of the buried sources on the grid plane. The *TDX* filter is defined as:

$$TDX = \tan^{-1} \left(\frac{THDR}{\left| \frac{\partial T}{\partial z} \right|} \right). \quad (5)$$

Ferreira *et al.* (2013) introduced the tilt angle of the total horizontal derivative (*TAHD*) filter for the qualitative interpretation of magnetic and gravity data. The filter uses maximum amplitude values for edge detection of potential field sources. The *TAHD* filter normalises the vertical gradient of the *THDR* by means of its total horizontal gradient amplitude. The *TAHD* filter is defined as:

$$TAHD = \tan^{-1} \left[\frac{\frac{\partial THDR}{\partial z}}{\sqrt{\left(\frac{\partial THDR}{\partial x} \right)^2 + \left(\frac{\partial THDR}{\partial y} \right)^2}} \right]. \quad (6)$$

The *TAHD* algorithm balances the signals from shallow and deep sources, and is a filter for edge detection even when the edges of the detected sources have low resolutions (Prasad *et al.*, 2022).

Eshaghzadeh *et al.* (2018) proposed the TA of the balanced total horizontal derivative (*TBHD*) filter. The *TBHD* algorithm normalises the vertical gradient of the balanced total horizontal derivative (*THDRB*) by means of its total horizontal gradient amplitude. The *TBHD* method is defined as:

$$TBHD = \tan^{-1} \left[\frac{\frac{\partial THDRB}{\partial z}}{\sqrt{\left(\frac{\partial THDRB}{\partial x} \right)^2 + \left(\frac{\partial THDRB}{\partial y} \right)^2}} \right] \quad (7)$$

where

$$THDRB = \frac{THDR}{K + \sqrt{[H_x(THDR)]^2 + [H_y(THDR)]^2 + THDR^2}} \quad (8)$$

In Eq. 8, H_x and H_y are the Hilbert transform of the $THDR$ algorithm in the X and Y directions, respectively. The K value is a constant value that controls the effectiveness of the method (Cooper, 2009; Eshaghzadeh *et al.*, 2018). The amplitude maxima are positioned over the horizontal lateral boundaries of the causative source frames; therefore, they can be used for edge detection of potential field data.

3. The Gompertz edge determination filter

This paper proposes an edge enhancement filter, based on the Gompertz function, to balance the horizontal lateral boundaries of potential field causative sources located at different depths and with high resolutions. The Gompertz function [GF , see e.g. Winsor (1932) and Iliev *et al.* (2017)] is almost identical in shape to the inverse tangent function commonly used for edge detection of gravity and magnetic field data. The GF , or improved TA of the balanced total horizontal derivative, is defined in Eq. 9:

$$GF = \exp \left\{ -K \times \exp \left[-\frac{\frac{\partial ITHDR}{\partial z}}{\sqrt{\left(\frac{\partial ITHDR}{\partial x}\right)^2 + \left(\frac{\partial ITHDR}{\partial y}\right)^2}} + 1 \right] \right\} \quad (9)$$

where

$$ITHDR = \frac{THDR^K}{2 + \sqrt{[H_x(THDR)]^2 + [H_y(THDR)]^2 + THDR^2}} \quad (10)$$

and the K value is a positive number, established by the interpreter, equal to, or greater than, one. The amplitude amount of the proposed filter is between zero and one, and the amplitude maxima are located on the edges of the anomaly sources. This filter can equalise the amplitudes of anomalies caused by structures, at different depths and with high resolutions. To evaluate the effectiveness of the proposed filter, a comparison was performed with other standard edge detector algorithms (e.g. $THDR$, ASA , TA , TM , TDX , $TAHD$, and $TBHD$). Therefore, the filter is applied to imposed synthetic models, Bishop synthetic models, and real data sets from the state of Georgia (U.S.A.) and the Gol-e-Gohar iron ore mine (Iran).

4. Evaluation of the K value

A two-dimensional model has been taken into consideration to study the role of K with different values, and its contribution to determining the edges and increasing resolution. A synthetic

gravity model consisting of three prisms, with different properties and buried at different depths, is used to evaluate the K value for the proposed source edge detector. The properties assigned to the bodies are shown in Fig. 1a. The calculated gravity effects are shown in Fig. 1b. The GF edge detection method is applied to the calculated gravity effects with increasing values from 0.5 to 11 (Figs. 1c to 1j). The results show that the amplitude response of the proposed filter is maximum over the edges. When the K value is one, the filter produces sharp edges that maintain their sharpness until the K value equals 10. The detected edge is unreliable and faulty if the K value is greater than 4. Therefore, to determine filter effectiveness, best results are obtained with a K value ranging from 1 to 4. In this study, a K value of 1.5 is set for all theoretical and field data models in the relation between the $TBHD$ and GF filters.

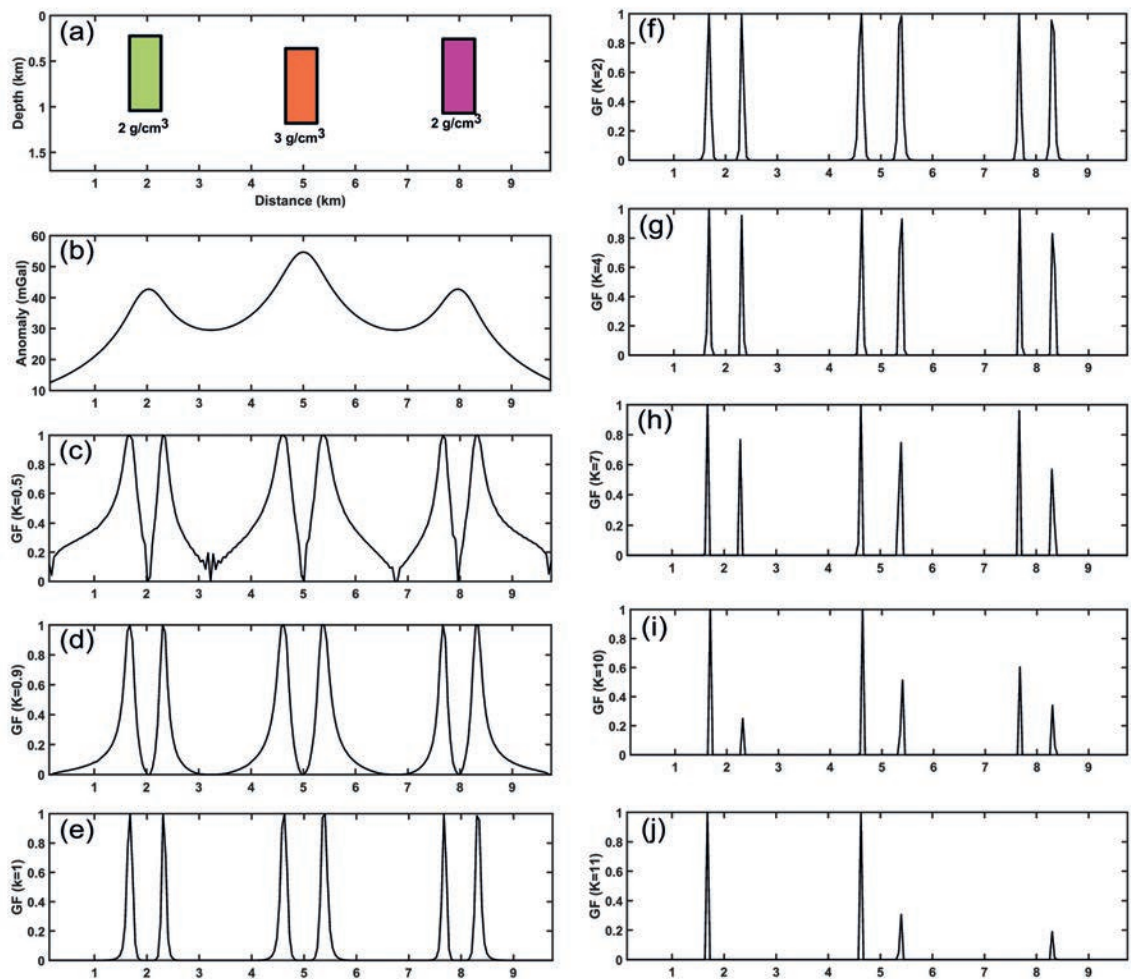


Fig. 1 - Evaluation of the K value in the GF over a synthetic gravity anomaly: a) schematic representation of the 2D synthetic model; b) response of the gravity anomaly over the three prismatic bodies. GF response at: c) $K = 0.5$, d) $K = 0.9$, e) $K = 1$, f) $K = 2$, g) $K = 4$, h) $K = 7$, i) $K = 10$, j) $K = 11$.

5. Theoretic model testing

This study considered noise-corrupted and noise-free synthetic gravity and magnetic models to evaluate the robustness of the *GF* edge detection filter, here following described in detail.

5.1. The prismatic models

5.1.1. The gravity model

Figs. 2a and 2b show the 3D and planer views of the gravity model, which includes seven prisms (A1, B1, C1, D1, E1, F1, and G1) with positive and negative density contrasts, two prisms with the same size but different density and depth (B1 and C1), two prisms with the same negative density contrast (C1 and D1), two prisms with the same positive density contrast (B1 and G1), and two prisms with the same depth (D1 and F1). The parameters of the synthetic model are listed in Table 1. The gravity anomaly of the synthetic model was produced at 200×200 km² grid nodes, with a 1-km spacing along the X and Y directions (Fig. 3a).

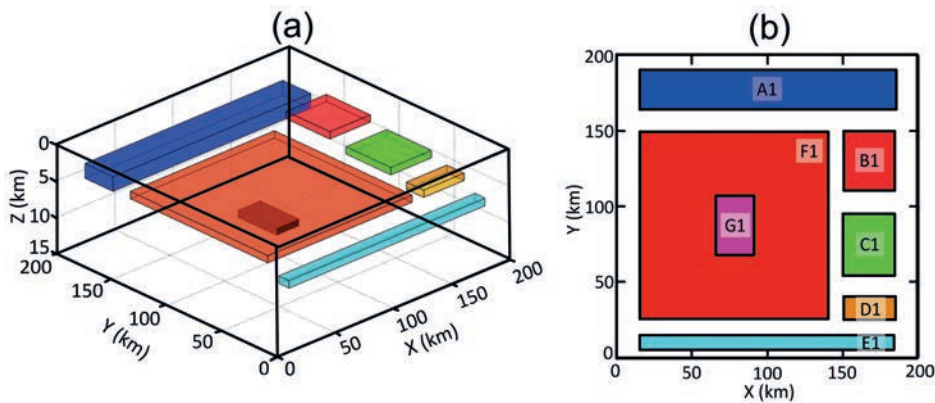


Fig. 2 - 3D representation of the synthetic gravity model (a) and top view of the synthetic gravity model with seven prisms (b).

Table 1 - The spatial and physical parameters of the synthetic gravity model.

Source/Label	A1	B1	C1	D1	E1	F1	G1
X-coordinates of the centre (km)	100	167	167	167	100	85	75
Y-coordinates of the centre (km)	178	130	75	32	10	88	75
Width (km)	25	35	35	13	10	125	20
Length (km)	160	40	40	35	160	125	35
Depth of top (km)	3	2	3	4	6	4	7
Depth of bottom (km)	5	3	4	5	7	5	8
Density contrast (g/cm ³)	-0.3	0.5	-0.5	-0.5	-1	0.6	0.5

As shown in Fig. 3b, the *THDR* method result is dominated by the strong amplitude responses of bodies A1, B1, C1, and F1, while the weak amplitude responses of bodies D1, E1, and G1 are

blurred and not clear. The *ASA* can detect the edges of bodies A1 and B1, whereas the filter resolution is insufficient to clearly delineate the edges of the other bodies (Fig. 3c). The *TA* filter successfully detects the edges of bodies A1, B1, C1, D1, and F1, but is less effective for bodies E1 and G1 (Fig. 3d). In addition, the *TM* algorithm produces false minimum contours in the output map (Fig. 3e). The *TDX* method provides results which are very similar to the *TM* edge detection method. The minimum amplitude of the *TM* filter indicates the location of the edges, while the *TDX* filter detects the source edges using the maxima. Similarly to the *TM* filter, the *TDX* filter produces false contours in the output map (Fig. 3f). For the deepest source (G1) and the thinnest source (E1), the lateral boundaries detected by the *TA*, *TM*, and *TDX* filters are shifted away from the edges, making the buried bodies appear larger than they actually are. The *TAHD*, *TBHD*, and *GF* filters can simultaneously balance the low and high amplitudes of the different sources, and the edges of the sources can be detected on the basis of their maximum values (Figs. 3g to 3i). The *TAHD*, *TBHD*, and *GF* filters are more accurate in estimating the source edges than the *THDR*, *ASA*, *TA*, *TM*, and *TDX* algorithms and prevent the generation of false horizontal

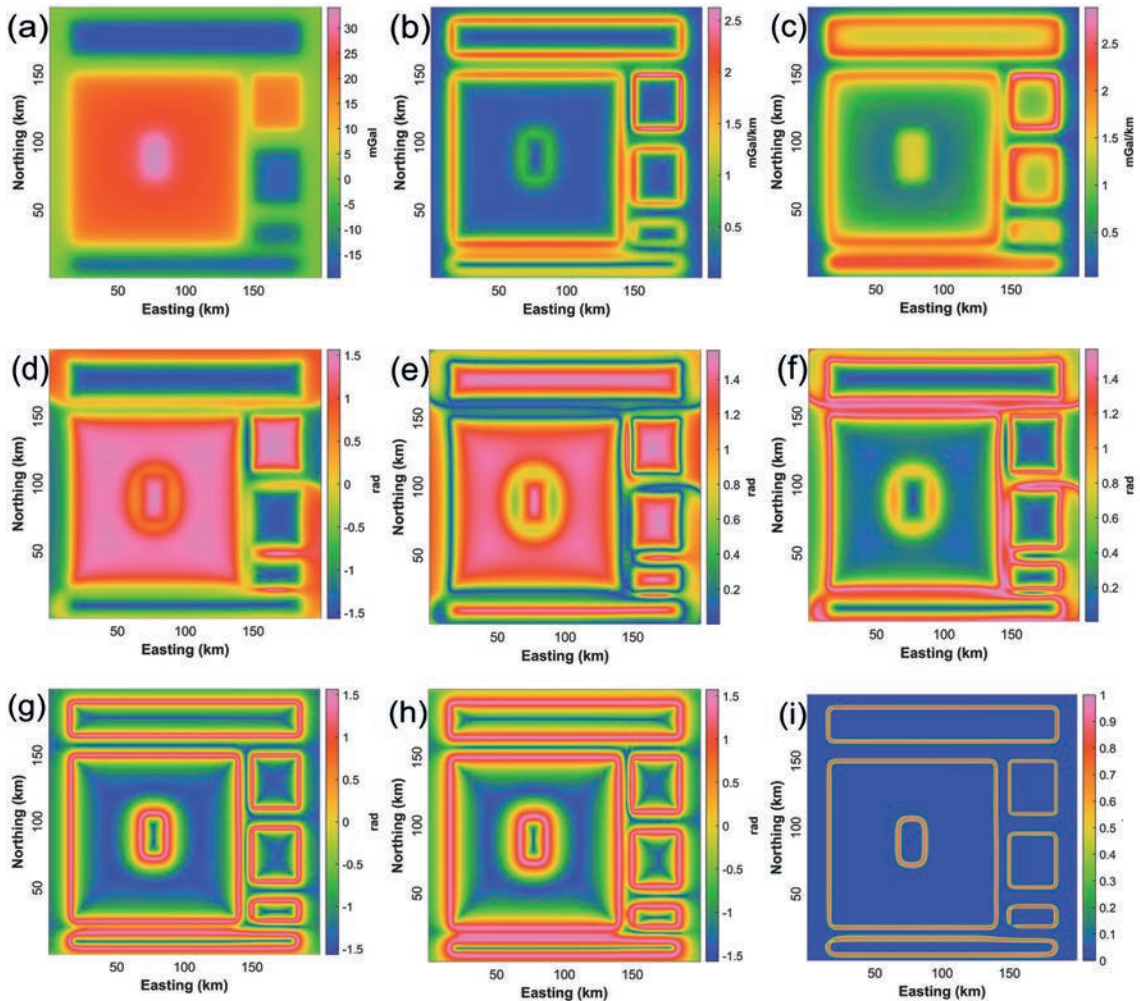


Fig. 3 - Comparison of results obtained with different filters: a) synthetic gravity model of the seven prisms with positive and negative density contrast; b) *THDR*; c) *ASA*; d) *TA*; e) *TM*; f) *TDX*; g) *TAHD*; h) *TBHD*; i) *GF*.

boundaries in the output image. However, the proposed *GF* filter can detect the edges of the buried structures with a higher resolution compared to the *TAHD* and *TBHD* filters, and can also equalise the amplitudes of the anomalies, caused by the structures at different depths, with positive and negative density contrast.

5.1.2. The gravity model with added noise

Fig. 4a shows the gravity anomaly caused by the seven prisms. A random noise, with amplitude equal to 3% of the anomaly amplitude, was added to this to investigate the noise effect as well. Before applying the edge detection methods, *THDR*, *ASA*, *TA*, *TM*, *TDX*, *TAHD*, *TBHD*, and *GF* methods, a 1-km upward continuation filter of the gravity field data was applied to attenuate the effects of random noise.

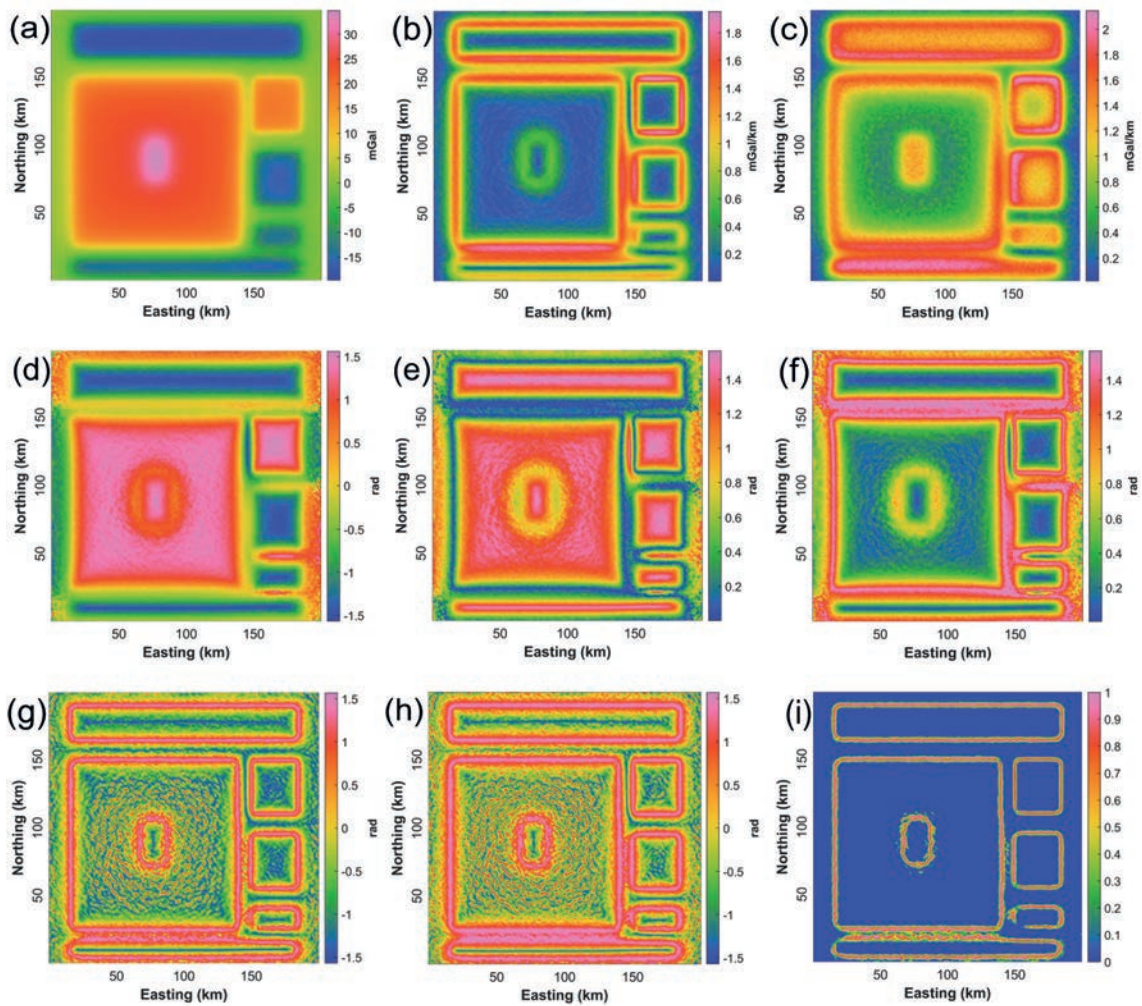


Fig. 4 - Comparison of results obtained with different filters: a) the gravity data of the synthetic model with random noise with amplitude equal to 3% of the anomaly amplitude; b) *THDR*; c) *ASA*; d) *TA*; e) *TM*; f) *TDX*; g) *TAHD*; h) *TBHD*; i) *GF*.

Strong amplitude anomalies dominate the results of the *THDR* and *ASA* filters, which cannot clearly detect the edges of weak amplitude anomalies (Figs. 4b and 4c). The *TA* filter efficiency is also low in determining the edges of deep and thin sources (Fig. 4d). Likewise, *TM* and *TDX* filters are unable to determine the horizontal boundaries of thin and deep sources (Figs. 4e and 4f). Figs. 4g and 4h show how the *TAHD* and *TBHD* methods are able to detect all source edges, but do not produce a high-resolution and clear image. The results obtained in using the *GF* filter (Fig. 4i) show that this algorithm is less dependent on the depth of the buried structures, and the delineated edges are clearer than those achieved with the *TAHD* and *TBHD* filters. Still, the *GF* edge detection filter does not produce false horizontal lateral boundaries.

5.1.3. The magnetic model

The synthetic magnetic model, consisting of four prismatic sources, is shown in Figs. 5a and 5b; and its relevant parameters are listed in Table 2. Similar to other edge detection methods (Alvandi *et al.*, 2022b; Prasad *et al.*, 2022), the proposed filter requires reduction to pole data; therefore, for all four prismatic bodies, the inclination and declination of the magnetic field are set to 90° and 0° , respectively. The total magnetic intensity is calculated on a 200×200 km² grid, with a 1-km grid spacing along the X and Y directions. Fig. 6a shows the synthetic magnetic anomaly generated by the negative and positive remnant magnetisation sources.

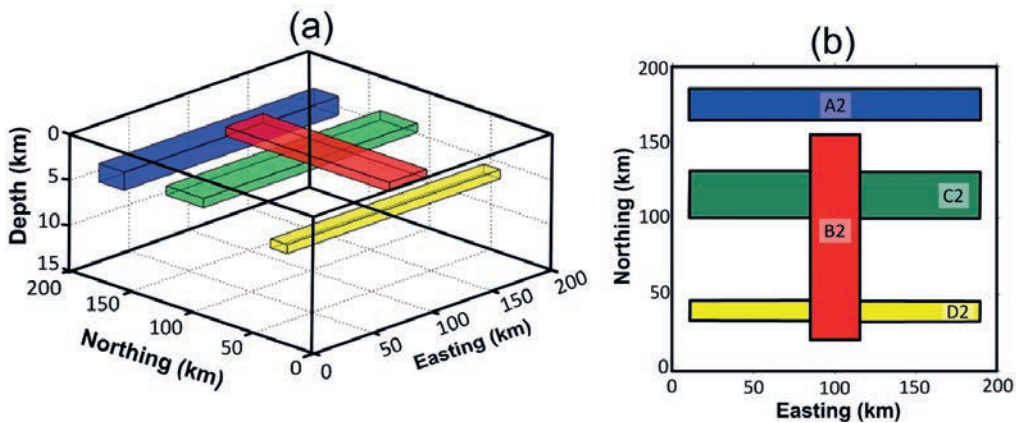


Fig. 5 - 3D representation of the synthetic magnetic model (a) and top view of the synthetic magnetic model (b).

Table 2 - The spatial and physical parameters of the synthetic magnetic model.

Source/Label	A2	B2	C2	D3
X-coordinates of the centre (km)	100	100	100	100
Y-coordinates of the centre (km)	175	88	115	39
Width (km)	20	30	30	12
Length (km)	180	135	180	180
Depth of top (km)	3	1	3	5
Depth of bottom (km)	5	2	4	6
Magnetisation (A/m)	1	1	-1	-0.5
Strike azimuth	0°	0°	0°	0°

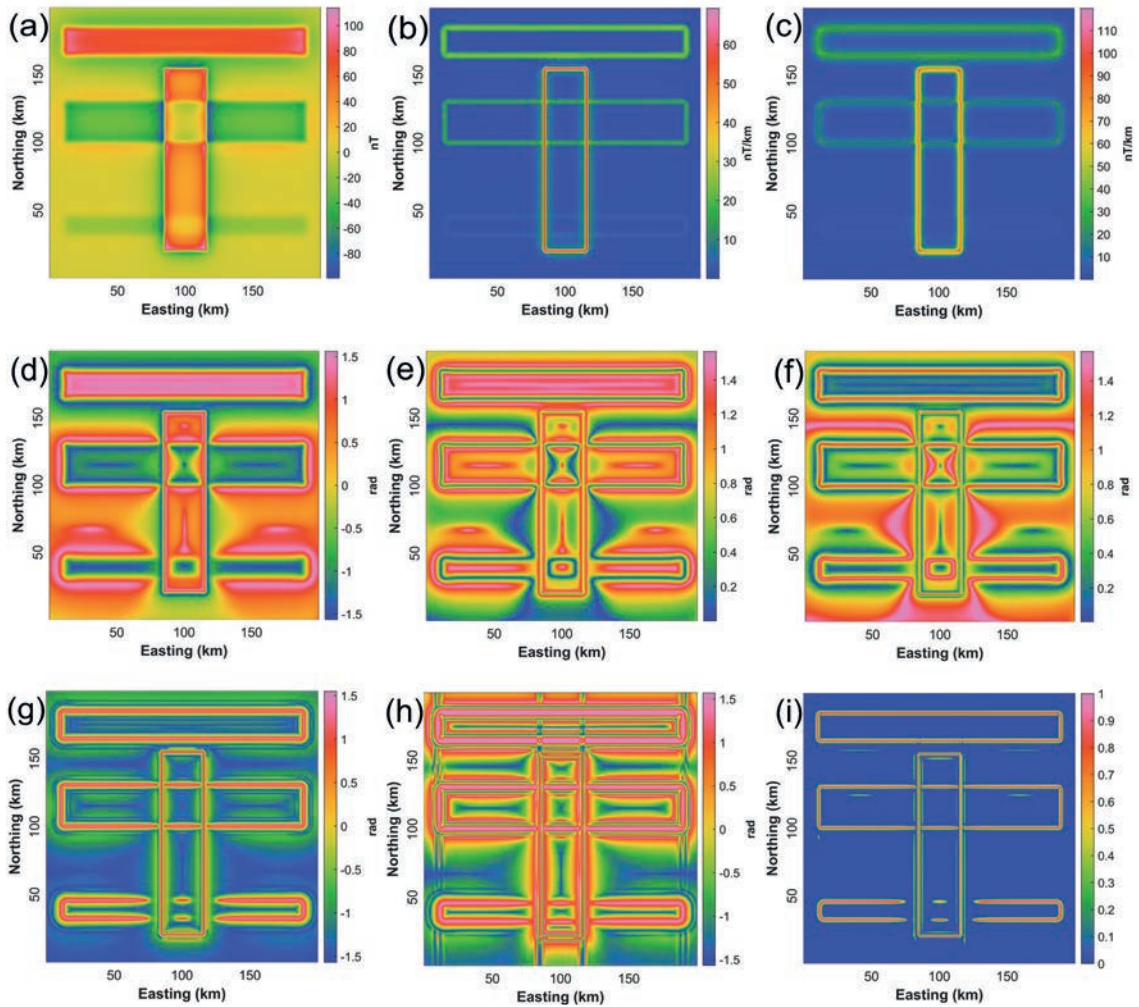


Fig. 6 - Comparison of results obtained with different filters: a) the magnetic synthetic model of the four prisms with positive and negative magnetisations; b) *THDR*; c) *ASA*; d) *TA*; e) *TM*; f) *TDX*; g) *TAHD*; h) *TBHD*; i) *GF*.

In this case, the *THDR*, *ASA*, *TA*, *TM*, *TDX*, *TAHD*, *TBHD*, and *GF* filters were applied. The results are shown in Figs. 6b to 6i. The results of the *THDR* method are given in Fig. 6b. The large amplitude response dominates the results due to the shallow source, B2, but the small amplitude responses due to the deeper sources, A2, D2, and C2, are blurred. The filter *ASA* shows distinct boundaries for the shallow source, B2, but the lateral boundaries become blurred with increasing depths (Fig. 6c). Figs. 6d to 6f show the results of the *TA*, *TM*, and *TDX* filter algorithms, respectively. Although the methods, in this case, outline the edges of the deep and shallow sources, they bring false and spurious horizontal boundaries between the sources. Fig. 6g shows the edges detected by the *TAHD* method. It is evident that the method provides maximum values over the horizontal lateral boundaries of the sources. Compared to results obtained with the other filters, the *TAHD* filter results are more even, clearer, and better, showing no false edges. Fig. 6h shows the results of the *TBHD* filter. In this case and unexpectedly, the method is less effective at highlighting the source edges, and it also introduces obvious additional false boundaries between the sources. Edge detection of the *GF* filter is shown in Fig. 6i. Compared

to the results of other edge detection filters, the *GF* filter stands out for producing balanced, clear, and refined horizontal boundaries between deep and shallow levels, and minimising interference. An intriguing feature of the *GF* method is that the maximum amplitude of the filter is positioned over the lateral boundary of the sources, and the edge is not displayed as larger.

5.1.4. The magnetic model with added noise

We applied the proposed filter to a magnetic model containing random noise with amplitude equal to 3% of the anomaly amplitude. The noisy anomaly is shown in Fig. 7a. A 1-km upward continuation distance filter, to stabilise the results, is used due to the high-level noise added to the data. Figs. 7b and 7c show the results of the *THDR* and *ASA* methods, respectively. It is obvious that the *THDR* and *ASA* filters cannot balance the differences in amplitudes. Figs. 7d to 7f show the results of the *TA*, *TDX*, and *TM* methods, respectively. The phase-based filters can equalise the strong and weak amplitudes but, also, create additional

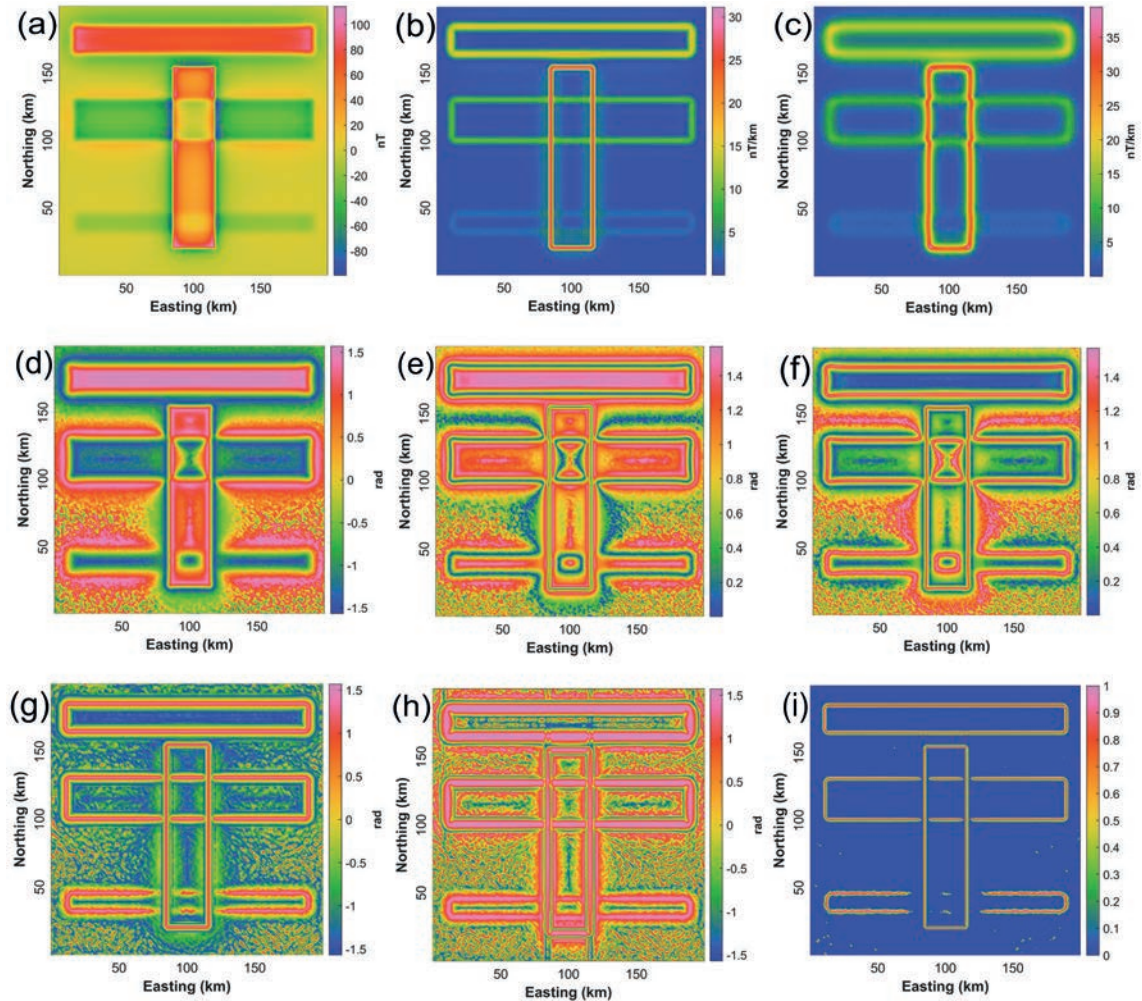


Fig. 7 - Comparison of results obtained with different filters: a) the magnetic data of the synthetic model with random noise with amplitude equal to 3% of the anomaly amplitude; b) *THDR*; c) *ASA*; d) *TA*; e) *TM*; f) *TDX*; g) *TAHD*; h) *TBHD*; i) *GF*.

spurious horizontal boundaries between sources and easily confuse the interpreter. Fig. 7g shows the results of the *TAHD* filter. The filter effectively detects edges and can prevent the generation of false boundaries in the output map. Fig. 7h shows the *TBHD* filter results. The false lateral boundaries appear in the output map, and proving that the *TBHD* filter cannot clearly delineate the source edges. The amplitude results of the *GF* filter are shown in Fig. 7i. Compared to the above results, the *GF* filter clearly outlines the edges of all four sources and improves visibility. It enhances the sharpness of the structures as well as the high resolution of the horizontal boundaries.

5.2. The Bishop complex synthetic model

To investigate the ability of edge detection filters while detecting deep and shallow structures, a case with complex sources, namely the Bishop synthetic gravity and magnetic models (Williams *et al.*, 2005; https://wiki.seg.org/wiki/Bishop_Model) is analysed. The Bishop complex model is a basement model developed on the real topography of a portion of the volcanic tablelands area north of Bishop, California, U.S.A. (Fairhead *et al.*, 2004; Reid *et al.*, 2005; Williams *et al.*, 2005; Florio, 2018). Several authors have used the Bishop model for edge detection from potential field data (Cooper, 2020; Dwivedi and Chamoli, 2021; Chen and Zhang, 2022). This case presents minor faults and two relatively long and large offset faults (striking N-S and E-W), which are indicated with the dashed lines in Fig. 8a (Florio, 2018). The unfaulted deep basin region is located in the south-eastern corner, and shallow structures are located NW of the Bishop gravity anomaly map (Williams *et al.*, 2005). In this study, noise-corrupted and noise-free Bishop models were considered to evaluate the robustness of the *GF* edge enhancement algorithm.

Fig. 8a shows the gravity anomaly produced by the Bishop model. Figs. 8b to 8i show the effect and capability of the various edge detection methods. As shown in Figs. 8b and 8c, the results of the *THDR* and *ASA* methods, respectively, are dominated by shallow-level sources, and the two main structures (main faults) appear blurred. *THDR* and *ASA* cannot balance small and large amplitudes at the same time. Figs. 8d to 8f show the data *TA*, *TM*, and *TDX* in Fig. 8a. All three filters cannot detect the edges of deep or thin structures well. In this case, *TA*, *TM*, and *TDX* filters are unable to locate the edges of the structures in the south-eastern corner of the edge detection map, thus leading to false edges in the output map. The *TAHD* and *TBHD* filters can equalise the edges of bodies with different depths, but the detected edges have lower resolutions compared to the *GF* filter (Figs. 8g and 8h). The *GF* algorithm provides high resolution compared to the other filters. It can balance the anomalies of shallow and deep sources, and extract the edges associated with the main and minor structures (Fig. 8i).

A random noise with amplitude equal to 3% of the anomaly amplitude was added to the Bishop model data to test the capability and quality of the edge determination filters. Fig. 9 shows the result of adding random noise to the synthetic model in Fig. 8a. A 1-km upward continuation filter is applied to Bishop model data to reduce the noise effect. Figs. 9b to 9i show the results of edge detection filters for up-warded anomalies that are shown in Fig. 9a. The results of the *THDR* and *ASA* edge detection methods, once again, indicate that the *THDR* and *ASA* methods are not suitable for detecting lineaments and lateral boundaries (Figs. 9b and 9c), and that the detected edges are diffused. In addition, the *TA*, *TM*, and *TDX* filters produce additional spurious edges and can easily confuse the interpreter (Figs. 9d to 9f). The results of the *TAHD* and *TBHD* algorithms are given in Figs. 9g and 9h, respectively. Compared to the above results, the *TAHD* and *TBHD* filters show the edges of all major and minor faults as well as those of other structures.

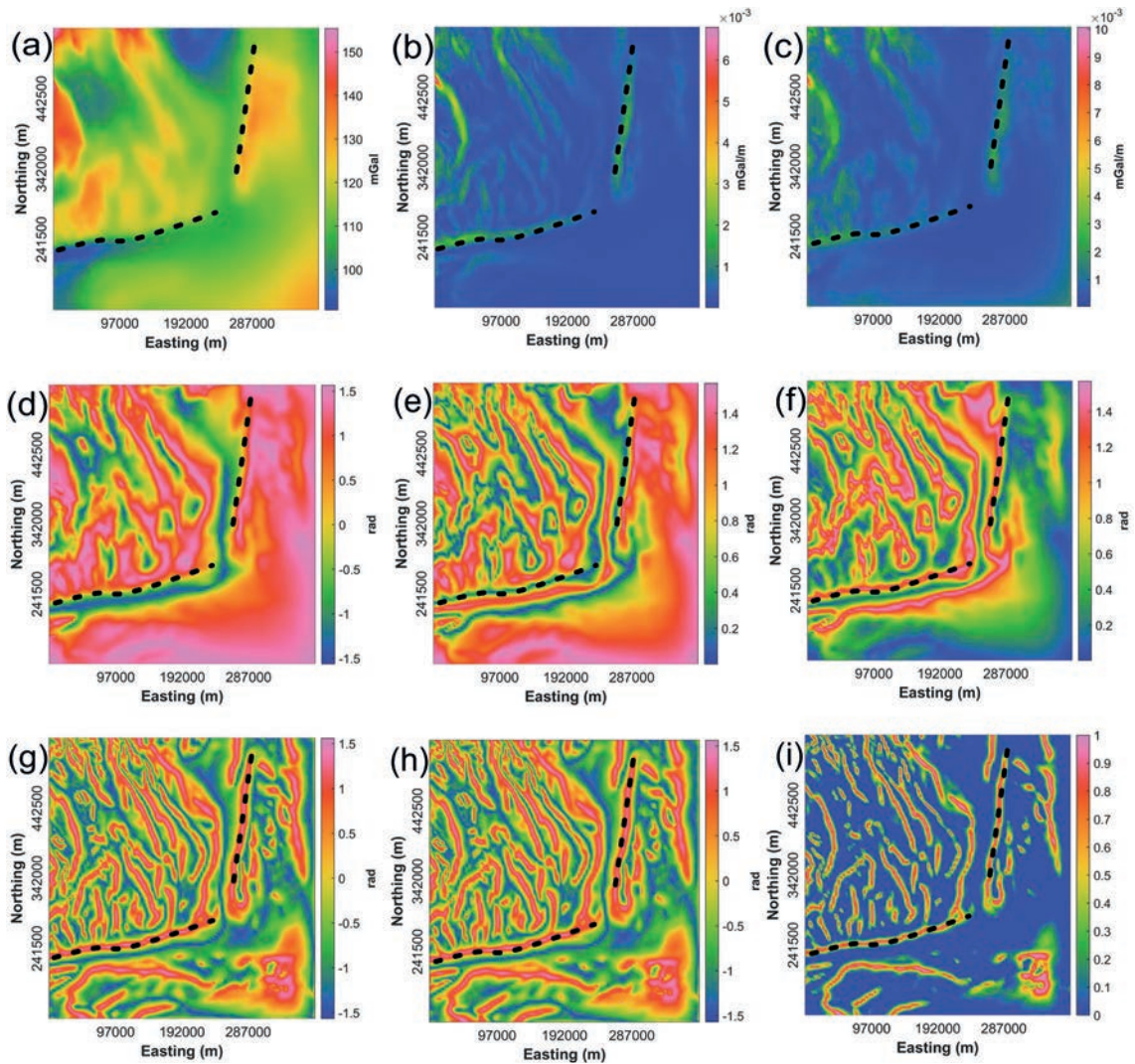


Fig. 8 - Comparison of results obtained with different filters: a) gravity field of the Bishop basement model (two large offset faults are indicated with the dashed lines); b) *THDR*; c) *ASA*; d) *TA*; e) *TM*; f) *TDX*; g) *TAHD*; h) *TBHD*; i) *GF*.

Fig. 9i shows the edges detected with the *GF* algorithm. The *GF* algorithm can simultaneously balance weak and strong amplitudes, thus avoid producing any false edges, and outputting a high-resolution edge detection map.

Fig. 10a shows the magnetic reduction to the pole of the magnetic anomaly produced by the Bishop model. Figs. 10b to 10i show the effect and capability of the different edge enhancement methods. The results obtained are similar to those of the gravity model in the previous section. Again, the *GF* filter is of better quality and is capable of detecting horizontal boundaries. Random noise with amplitude equal to 3% of the anomaly amplitude was added to the magnetic model data to investigate the ability and quality of the edge enhancement filters. Fig. 11 shows the result obtained with the addition of random noise to the synthetic model in Fig. 10a. A 1-km upward continuation filter is applied to the magnetic model data, before the horizontal boundaries determination filter, thus reducing the random noise effect. Figs. 11b to

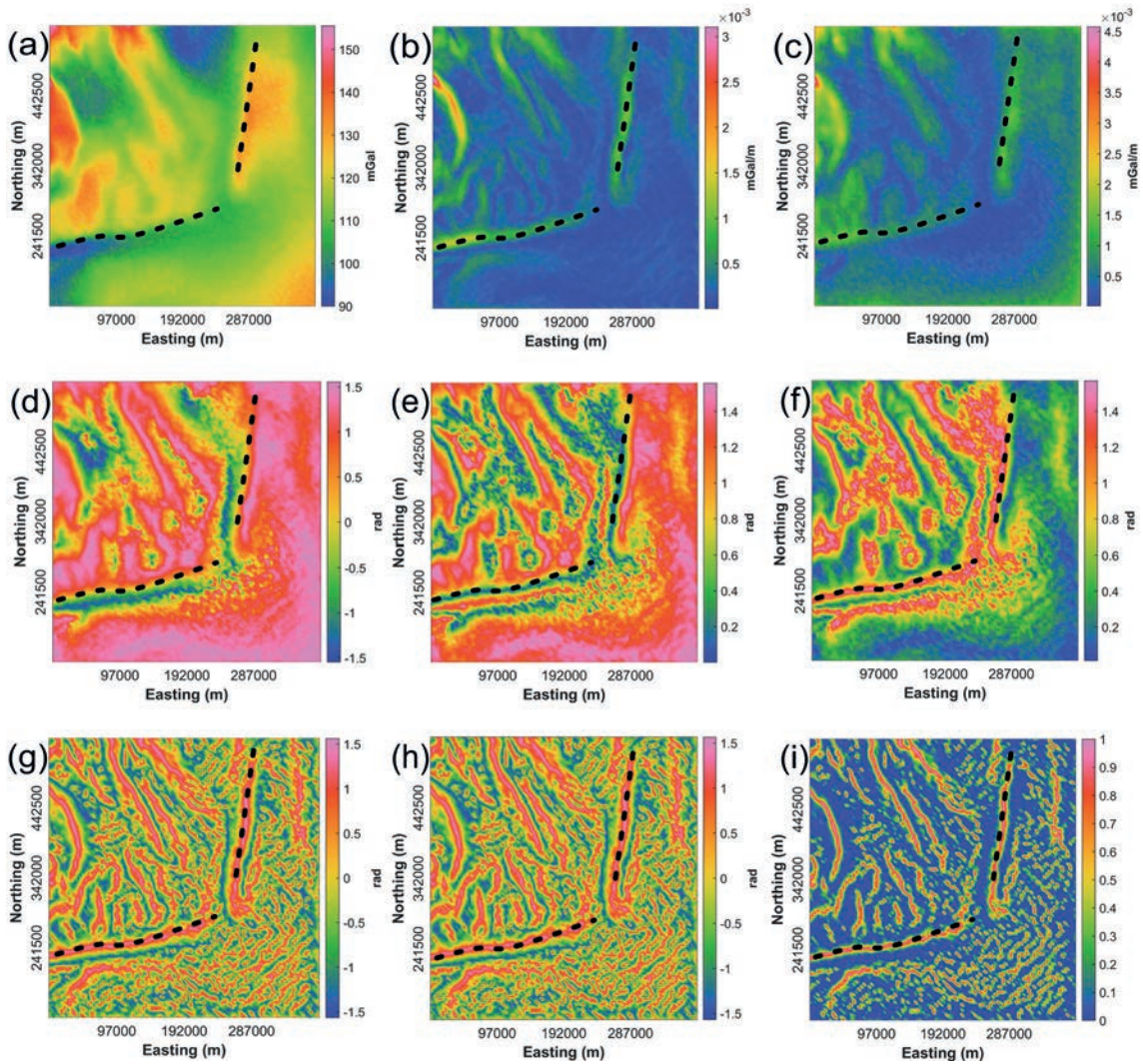


Fig. 9 - Comparison of results obtained with different filters: a) gravity data of the Bishop synthetic model with random noise with amplitude equal to 3% of the anomaly amplitude; b) *THDR*; c) *ASA*; d) *TA*; e) *TM*; f) *TDX*; g) *TAHD*; h) *TBHD*; i) *GF*.

11i show the edge detection filter results after the data upward continuation filter in Fig. 11a. The *GF* algorithm can simultaneously equalise weak and strong amplitudes, thus avoiding the production of any false lateral boundaries, and outputting a high-resolution edge detection image.

6. Real aeromagnetic data

In this section, the practical applicability of the proposed filter is demonstrated with the interpretation of high-resolution aeromagnetic data belonging to a part of the state of Georgia, in south-eastern United States (Fig. 12a). The area lies between longitudes 82.80° and 84.30° W and latitudes 32.20° and 34.50° N, i.e. the study area is located in two different geological

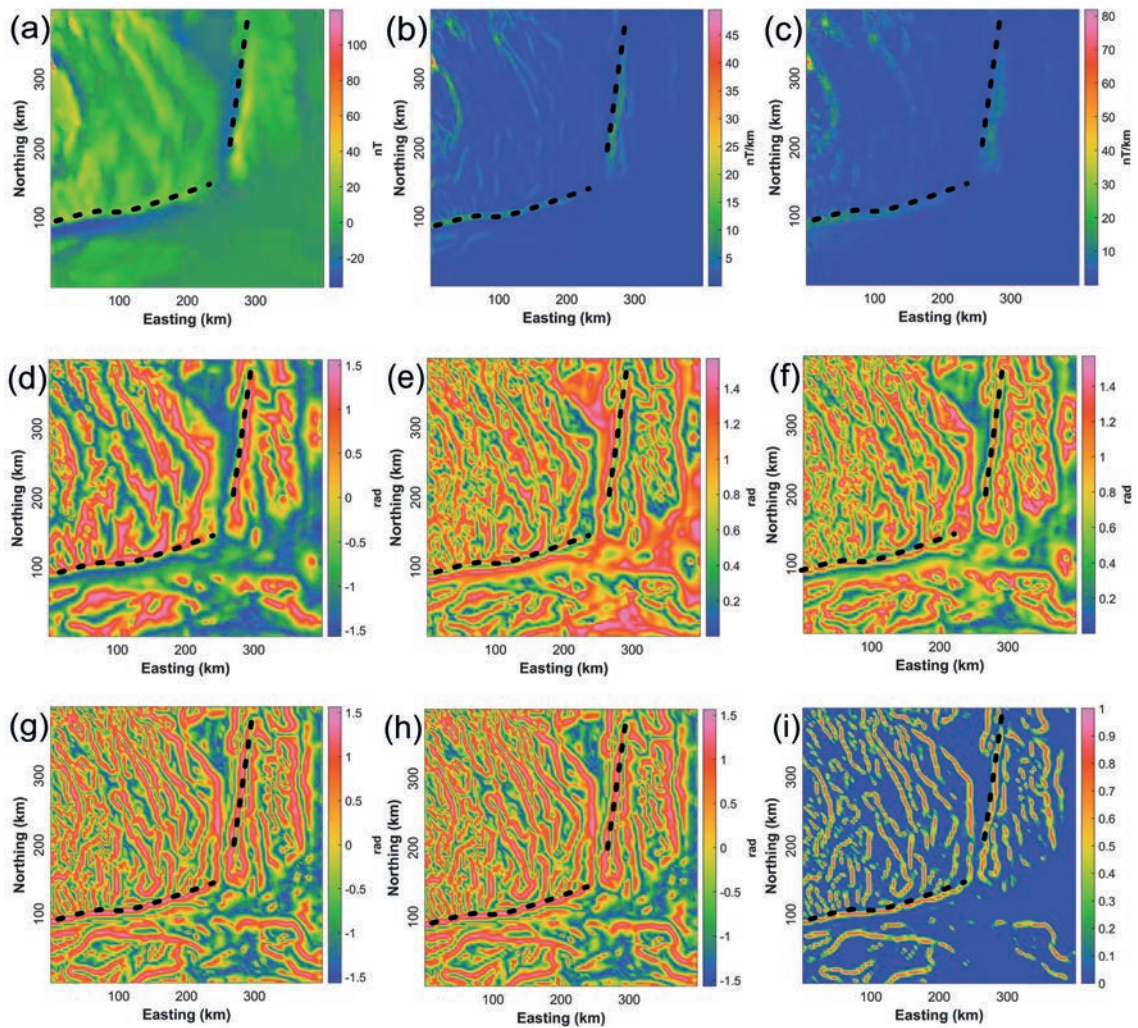


Fig. 10 - Comparison of results obtained with different filters: a) Bishop bedrock model magnetic field (two large offset faults are indicated with the dashed lines); b) *THDR*; c) *ASA*; d) *TA*; e) *TM*; f) *TDX*; g) *TAHD*; h) *TBHD*; i) *GF*.

areas, Piedmont and the Coastal Plain. The fall line (FL) is the border between Piedmont and the Coastal Plain (Fig. 12b). The Piedmont geological region consists of igneous and metamorphic rocks such as schist, amphibolite, gneiss, and granite (Hack, 1982). The Coastal Plain in Georgia is part of a geological region composed of sedimentary rocks deposited from the Late Cretaceous to Holocene periods. A simplified geological map of the study area (modified by Lawton *et al.*, 1976; Pickering and Murray, 1976), on a 1:500,000 scale, is shown in Fig. 12b. The Piedmont region presents a complex geological structure with numerous faults and dikes. Determination of the location and identification of faults and dikes in Georgia, using regional aeroradioactivity, aeromagnetic mapping, and seismic reflection studies, has increased the number of faults that were difficult to identify without the use of geophysical methods (Bentley *et al.*, 1974; Alarifi, 2022). The major faults of Brevard (in the northern part of the map), Towaliga-Lowndesville (in the central part of the Piedmont zone) and Bartletts Ferry (near the fall line) are marked on the geological map (Fig. 12b).

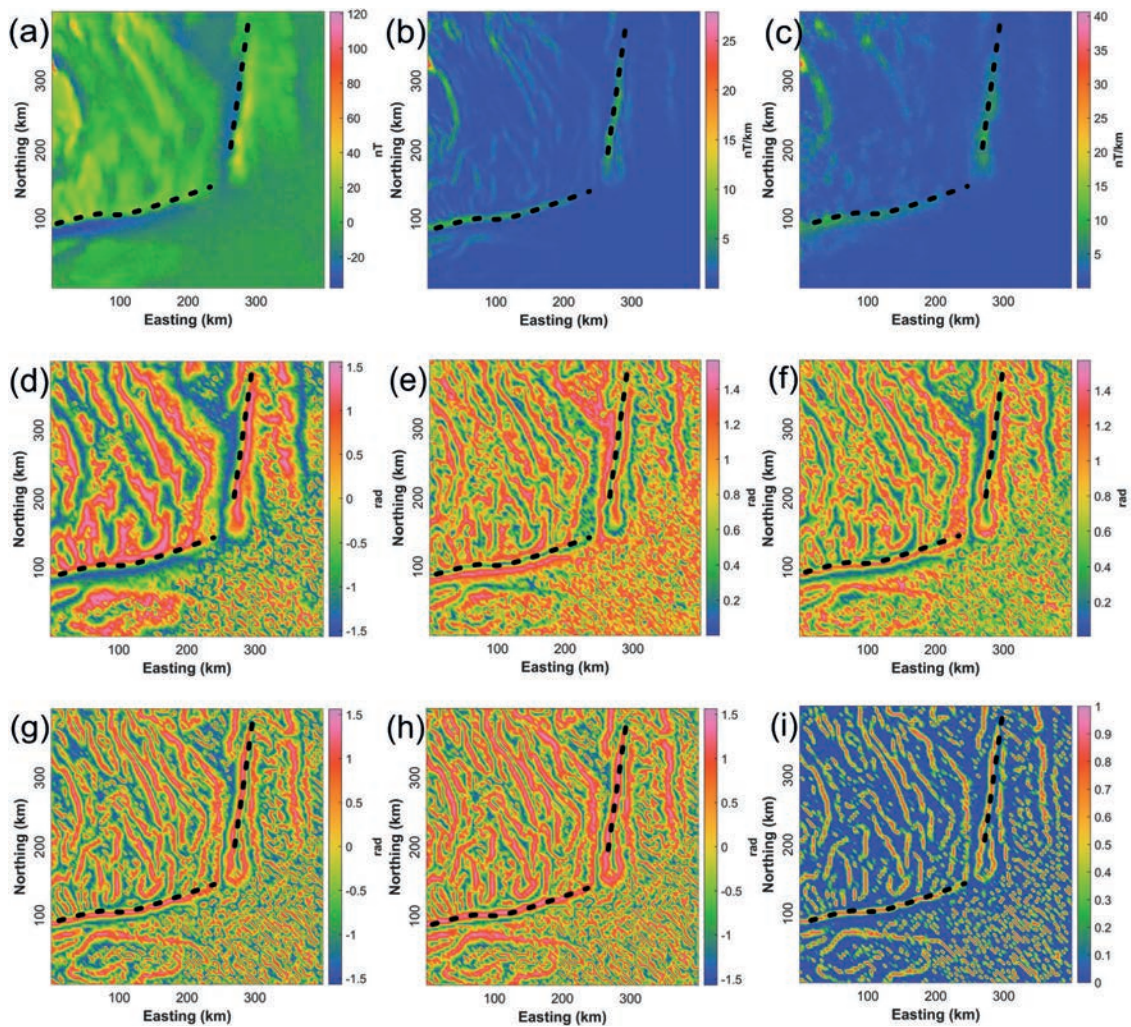


Fig. 11 - Comparison of results obtained with different filters: a) magnetic field of the Bishop basement model with random noise with amplitude equal to 3% of the anomaly amplitude (two large offset faults are indicated with the dashed lines); b) *THDR*; c) *ASA*; d) *TA*; e) *TM*; f) *TDX*; g) *TAHD*; h) *TBHD*; i) *GF*.

Fig. 13a shows the aeromagnetic data of the study area (Daniels, 1974, 2001; Alarifi, 2022). In this study, aeromagnetic data were RTP, and a 2-km upward continuation filter was applied to the RTP anomaly maps before computing the edge determination filters in order to reduce the noise effect and produce smoother edge determination maps. As in the previous section, we compared the *GF* filter with the following edge determination filters: *THDR* (Fig. 13b), *ASA* (Fig. 13c), *TA* (Fig. 13d), *TM* (Fig. 13e), *TDX* (Fig. 13f), *TAHD* (Fig. 13g), and *TBHD* (Fig. 13h). As expected, the *THDR* and *ASA* filters are unsuccessful in determining the horizontal boundary of structures (Figs. 13b and 13c). Fig. 13d shows the results obtained by applying the *TA* edge enhancement filter to the aeromagnetic data. The *TA* map shows the presence of the major BF, TLF, and BFF faults, but other geological structures are blurred or unclear. Figs. 13e and 13f show the results obtained by applying *TM* and *TDX* filters, respectively. Both are effective in equalising amplitudes, but the horizontal lateral boundaries obtained with the *TM* and *TDX* methods are, to some extent, blurred. The horizontal lateral boundaries are correlated in all three edge detection

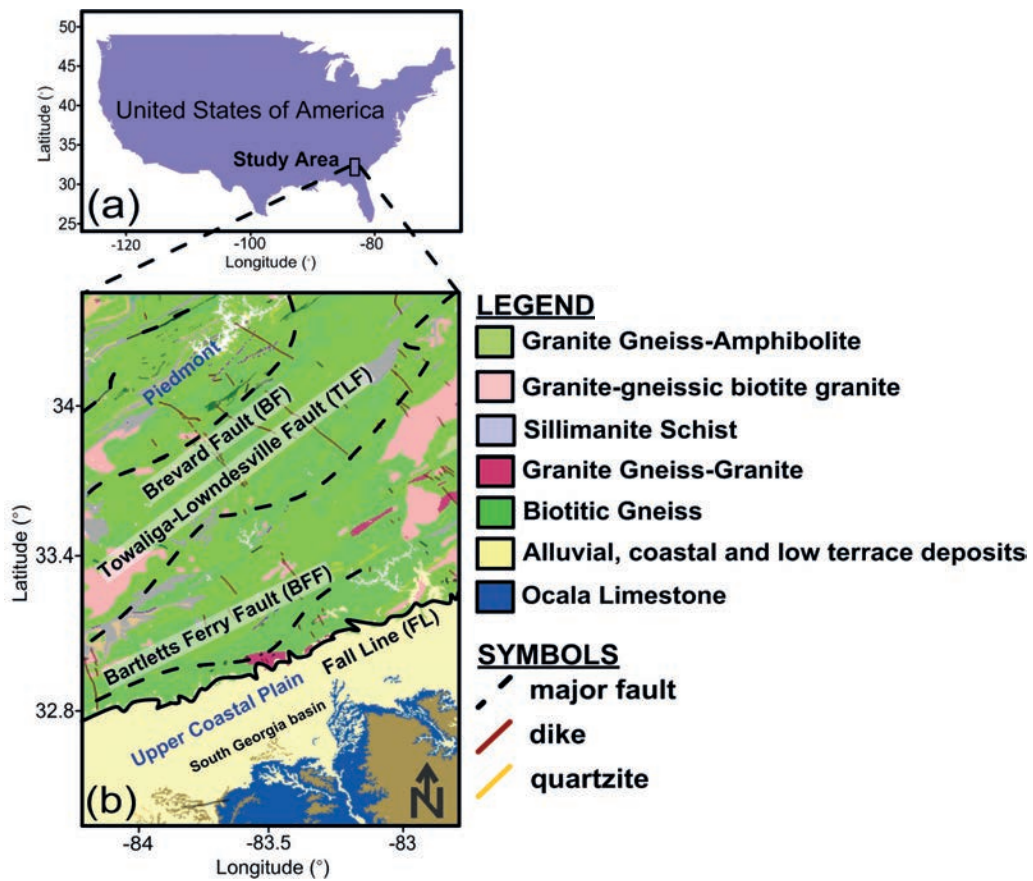


Fig. 12 - Location and simplified geological map of the study area (Lawton *et al.*, 1976; Bajgain, 2011; Pickering and Murray, 1976).

methods, TA , TM , and TDX , and this also complicates the interpretation. Figs. 13g and 13h show the results of the $TAHD$ and $TBHD$ filters, respectively. These results allow us to highlight anomalies at the edges of buried sources and provide evidence for determining faults and dikes. In this case, however, the $TBHD$ filter makes the sources seem bigger than they are. The main feature of the GF algorithm is the production of more subtle geologic features, and this is more effective for a qualitative interpretation of the study area. In this case, the peaks of the GF show a good correlation with the primary faults in the area (Fig. 13i).

7. Ground-based gravity data

In this section, the practicality of the GF filter is demonstrated by interpreting ground-based gravity field data from the Gol-e-Gohar iron ore mine in Kerman province, Iran (Fig. 14a). Iron ores are widely distributed in different regions of Iran, including central Iran (Choghart, Chadormelo, and Jalalabad), Sanandaj-Sirjan zone (Gol-e-Gohar-Sirjan and Shamsabad-Arak), eastern Iran (Sangan-Khaf), and some areas such as Bandar Abbas, Zanzan, and Semnan (Alvandi *et al.*, 2022a), while iron deposits are significant in terms of reserves in the Gol-e-Gohar region in Sirjan. The Gol-e-Gohar mining complex, with its rich iron ore mines, is located 50 km SW

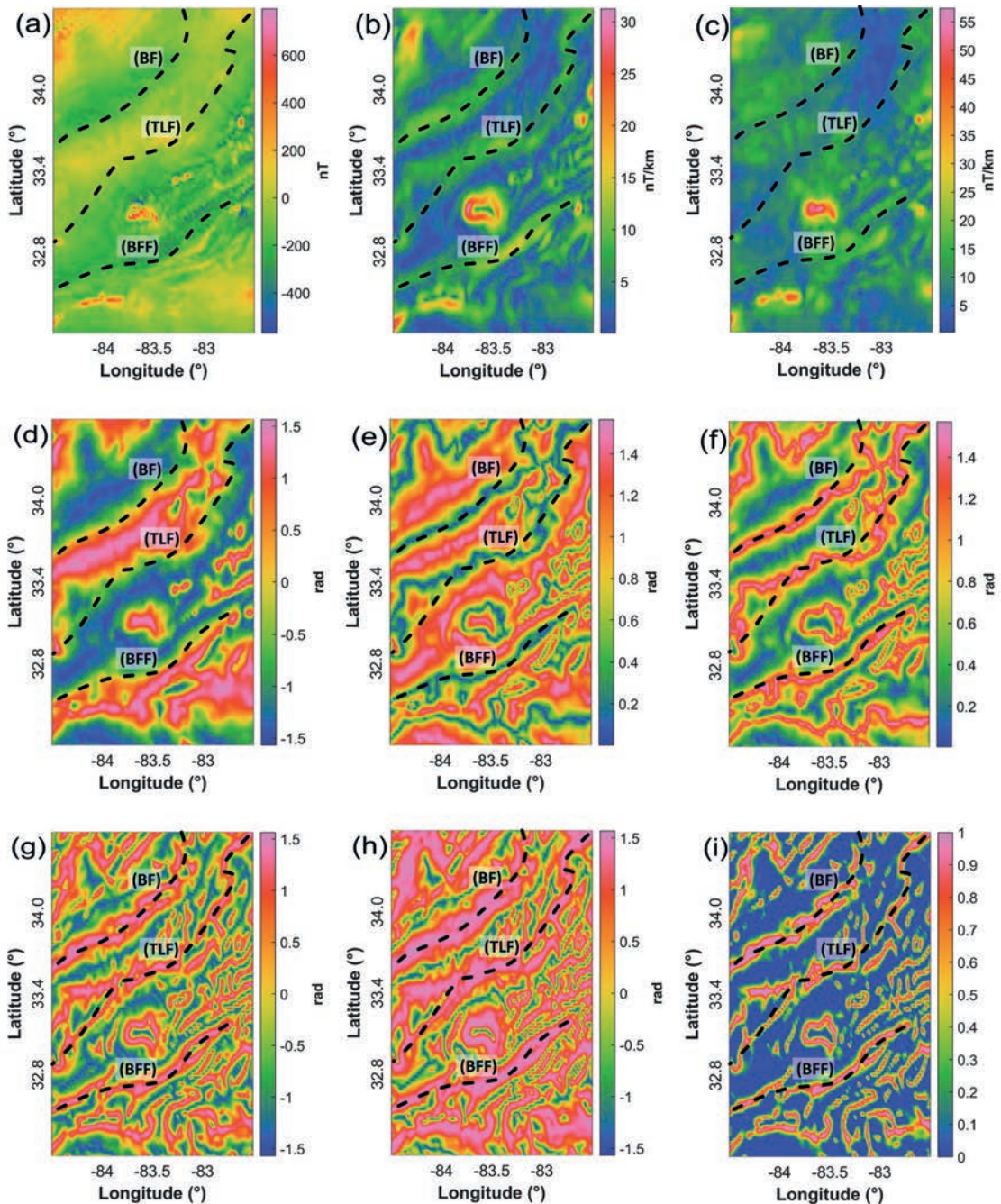


Fig. 13 - Comparison of results obtained with different filters: a) aeromagnetic data of the Georgia area; b) *THDR*; c) *ASA*; d) *TA*; e) *TM*; f) *TDX*; g) *TAHD*; h) *TBHD*; i) *GF*. BF = Brevard fault, TLF = Towaliga-Lowndesville fault, BFF = Bartletts Ferry fault.

of the city of Sirjan in Kerman province (approximately 29° N, 55° E) (Shahba *et al.*, 2017), and is one of the most important active mining poles in the Middle East. The Gol-e Gohar iron ore deposit is located in six separate anomalies, with a reserve of about 1,200 million tons in a range approximately 10 km long and 4 km wide. The effectiveness of edge detection methods

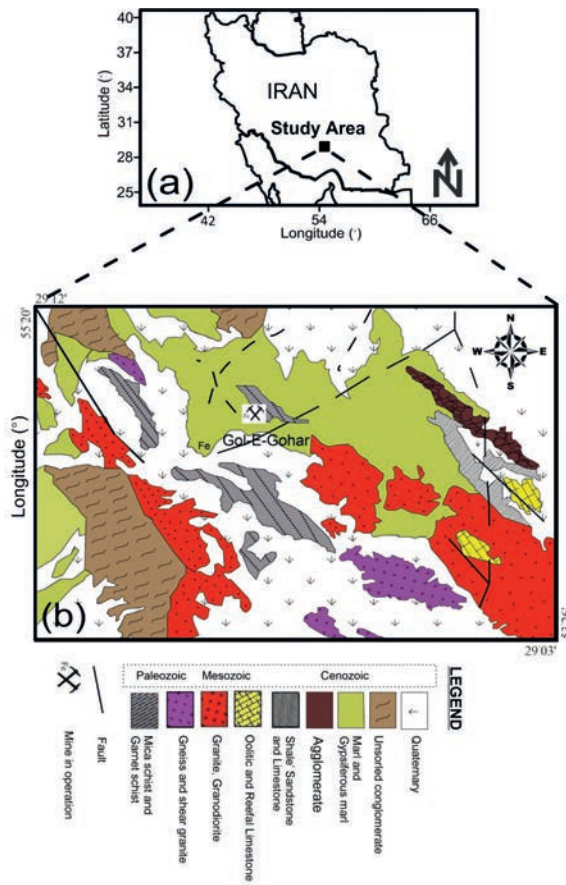


Fig. 14 - Geological map of Gol-e-Gohar with the position of the Gol-e-Gohar mine (Mahmoudi *et al.*, 2017; Behnam and Ramazi, 2019).

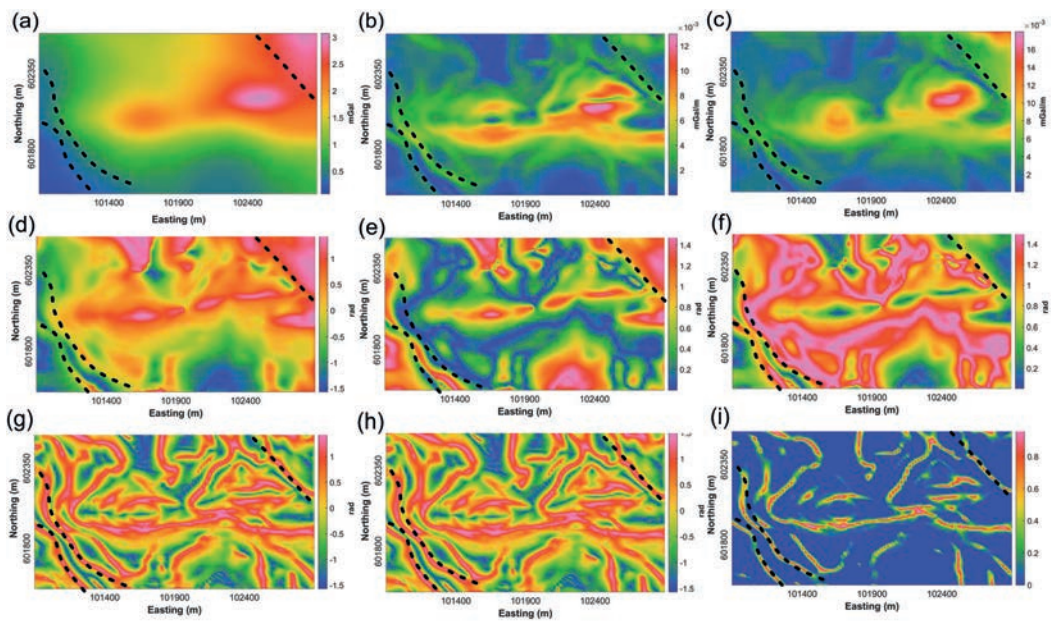


Fig. 15 - Comparison of results obtained with different filters: a) gravity data of the Gol-e-Gohar area; b) *THDR*; c) *ASA*; d) *TA*; e) *TM*; f) *TDX*; g) *TAHD*; h) *TBHD*; i) *GF*.

has been compared to delineate the geological structures of Gol-e Gohar iron ore mine No. 2. The simplified geological map of the Gol-e-Gohar area, the distribution of rock units and the major structural elements are shown in Fig. 14. To reduce the noise effect and produce smoother edge detection maps, a 20-m upward filter was applied to the gravity anomaly maps before calculating the edge detection methods. Fig. 15 shows the application of the different edge detection methods to the gravity field model. The gravity anomaly map of the Gol-e-Gohar mine is shown in Fig. 15a.

The large amplitudes dominate the *THDR* and *ASA* maps, and other detected buried sources are blurred, rendering the interpretation of the deep structures difficult (Figs. 15b and 15c). The *TA*, *TM*, *TDX*, *TAHD*, and *TBHD* maps (Figs. 15d to 15h) show strong signatures of faults and structures. In this case, however, the structural trends cannot be clearly identified using the *TA*, *TM*, and *TDX* filters. *TAHD* and *TBHD* are powerful methods that enable small and large amplitude signals to be balanced simultaneously. Fig. 15i shows the results obtained by applying the *GF* method to the Gol-e-Gohar gravity data set: the *GF* filter simultaneously balances the amplitude of large and small anomalies and, compared to the previously tested methods, is very effective in identifying geological structures.

8. Conclusions

We presented a high-resolution filter for determining field data edges. The filter was tested on synthetic gravity and magnetic data and field data from the U.S.A. and Iran. The comparison of the results proved that the *GF* algorithm can simultaneously balance the edges of different body sources at shallower and deeper depths, and the resolution of the causative source edges provided is better than that obtained with various conventional methods. Moreover, the horizontal boundaries of complex and imposed models can be clearly and accurately delineated. In this study, by applying various edge detection filters to the aeromagnetic data, the location and horizontal boundaries of the primary faults in the pediment zone, and some expected contacts and faults hidden beneath the coastal sediments in the upper coastal plain, were determined. Various edge detection filters were also applied to the gravity field data. The *GF* map clearly shows the trend of Gol-e-Gohar mine No. 2 and other buried structures. The *GF* filter is of better quality and provides reasonable accuracy and resolution for determining the boundaries of the geological structures. In addition, this filter is able to determine the edges of the buried geological structures by using potential field data without drawing additional and false boundaries. The images output using the *GF* filter can significantly help the interpreter in delivering a qualitative interpretation.

Acknowledgments. The authors thank the United States Geological Survey (USGS) for permission to use the geological map and aeromagnetic data in Figs. 12 and 13a, and the Iranian Mines & Mining Industries Development & Renovation (IMIDRO) for permission to use the gravity data and geological map from the Gol-e-Gohar area in Figs. 14 and 15a. The authors also wish to express their gratitude to Guy Flanagan (independent consultant, Albuquerque, NM, U.S.A.) for the help and assistance in collecting and interpreting the Bishop data, and to Giovanni Florio (University of Naples Federico II, Italy) for preparing Figs. 8a and 10a.

REFERENCES

Alarifi S.S.; 2022: *Structural implications of potential field data on southeastern North America*. J. Geophys. Eng., 19, 142-156, doi: 10.1093/jge/gxac005.

- Alvandi A., Toktay H.D. and Nasri S.; 2022a: *Application of direct source parameter imaging (direct local wave number) technique to the 2D gravity anomalies for depth determination of some geological structures, for depth determination of some geological structures*. Acta Geophys., 70, 659-667, doi: 10.1007/s11600-022-00750-6.
- Alvandi A., Toktay H.D. and Pham L.T.; 2022b: *Capability of improved logistics filter in determining lateral boundaries and edges of gravity and magnetic anomalies Tuzgolu area Turkey*. Iran. J. Min. Eng., 17, 56, 57-72, doi: 10.22034/ijme.2022.538984.1889, (in Persian).
- Alvandi A., Toktay H.D. and Pham L.T.; 2022c: *Interpretation of gravity data using logistic function and total horizontal gradient (LTHG) - A case study: Charak anticline*. J. Res. Appl. Geophys. (JRAG), 17, 402-410, doi: 10.22044/jrag.2022.11430.1325, (in Persian).
- Bajgain S.; 2011: *Gravity and magnetic modeling of basement beneath Alabama Gulf Coastal Plain*. M.S. Thesis in Geology and Geography, Auburn University, Auburn, AL, USA, 88 pp.
- Behnam S. and Ramazi H.; 2019: *Interpretation of geomagnetic data using power spectrum and 3D modeling of Gol-e-Gohar magnetic anomaly*. J. Appl. Geophys., 171, 103829, 8 pp., doi: 10.1016/j.jappgeo.2019.103829.
- Bentley R.O., Higgins M.W., Pickering S.M., Grant W.H., Zietz I. and Neathery T.L.; 1974: *Preliminary interpretation of an aeromagnetic map of most of the central and southern Georgia Piedmont*. Geol. Soc. Am. Abstr. with Programs, 6, 333-385.
- Chen A.G., Zhou T.F., Liu D.J. and Zhang S.; 2017: *Application of an enhanced theta-based filter for potential field edge detection: a case study of the Luzong ore district*. Chin. J. Geophys., 60, 203-218.
- Chen T. and Zhang G.; 2022: *NHF as an edge detector of potential field data and its application in the Yili basin*. Miner., 12, 149, doi: 10.3390/min12020149.
- Cooper G.R.J.; 2009: *Balancing images of potential field data*. Geophys., 74, L17-L20.
- Cooper G.R.J.; 2020: *A modified enhanced horizontal derivative filter for potential field data*. Explor. Geophys., 51, 549-554, doi: 10.1080/08123985.2020.1725386.
- Cooper G.R.J. and Cowan D.R.; 2006: *Enhancing potential field data using filters based on the local phase*. Comput. Geosci., 32, 1585-1591.
- Cordell L. and Grauch V.J.S.; 1985: *Mapping basement magnetization zones from aeromagnetic data in the San Juan basin, New Mexico*. In: Hinze W.J. (ed), The Utility of Regional Gravity and Magnetic Anomaly Maps, Society of Exploration Geophysicists, pp. 181-197, doi: 10.1190/1.0931830346.ch16.
- Daniels D.L.; 1974: *Geologic interpretation of geophysical maps, central Savannah River area, South Carolina and Georgia*. U.S. Department of the Interior, U.S. Geological Survey, Geophysical Investigations, Reston, VA, USA, Map GP-893, 10, doi: 10.3133/gp893.
- Daniels D.L.; 2001: *Georgia aeromagnetic and gravity maps and data: a web site for distribution of data*. U.S. Department of the Interior, U.S. Geological Survey Publication, Reston, VA, USA, Open-File Report 2001-106, doi: 10.3133/ofr01106.
- Dwivedi D. and Chamoli A.; 2021: *Source edge detection of potential field data using wavelet decomposition*. Pure Appl. Geophys., 178, 919-938, doi: 10.1007/s00024-021-02675-5.
- Eldosouky A.M.; 2019: *Aeromagnetic data for mapping geologic contacts at Samr El-Qaa area, north eastern Desert, Egypt*. Arabian J. Geosci., 12, 2 pp., doi: 10.1007/s12517-018-4182-2.
- Eshaghzadeh A., Dehghanpour A. and Kalantari R.A.; 2018: *Application of the tilt angle of the balanced total horizontal derivative filter for the interpretation of potential field data*. Boll. Geof. Teor. Appl., 59, 161-178.
- Fairhead J.D., Williams S.E. and Flanagan G.; 2004: *Testing magnetic local wavenumber depth estimation methods using a complex 3D test model*. In: Expanded Abstracts 74th Annual International Meeting, Society of Exploration Geophysicists, Houston, TX, USA, pp. 742-745.
- Fedi M. and Florio G.; 2001: *Detection of potential fields source boundaries by enhanced horizontal derivative method*. Geophys. Prospect., 49, 40-58.
- Ferreira F.J.F., de Souza J., Bongiolo A.B.S. and de Castro L.G.; 2013: *Enhancement of the total horizontal gradient of magnetic anomalies using the tilt angle*. Geophys., 78, J33-J41.
- Florio G.; 2018: *Mapping the depth to basement by iterative rescaling of gravity or magnetic data*. J. Geophys. Res. Solid Earth, 123, 9101-9120, doi: 10.1029/2018JB015667.
- Hack J.T.; 1982: *Physiographic divisions and differential uplift in the Piedmont and Blue Ridge*. U.S. Department of the Interior, U.S. Government Printing Office, Washington, DC, USA, Geological Survey professional paper 1265, 49 pp.

- Iliev A., Kyurkchiev N. and Markov S.; 2017: *A note on the new activation function of Gompertz type*. *Biomath. Commun.*, 4, 1-20, doi: 10.11145/10.11145/BMC.2017.10.201.
- Lawton D.E., Moye F.J., Murray J.B., O'Connor B.J., Penley H.M., Sandrock G.S., Marsalis W.E., Friddell M.S., Hetrick J.H., Huddleston P.F., Hunter R.E., Mann W.R., Martin B.F., Pickering S.M., Schneeberger F.J., and Wilson J.D.; 1976: *Geologic Map of Georgia*. Georgia Geological Survey, Georgia Department of Natural Resources, Geologic and Water Resources Division, Atlanta, GA, USA, Scale 1:500,000.
- Mahmoudi S., Mahmoudi A. and Mehrabi B.; 2017: *Microstructure and geochemical evidences for genesis of the Gol-e-Gohar iron deposit*. *J. Econ. Geol.*, 9, 463-481, doi: 10.22067/econg.v9i2.45322, (in Persian).
- Miller H.G. and Singh V.; 1994: *Potential field tilt - a new concept for location of potential field sources*. *J. Appl. Geophys.*, 32, 213-217.
- Nasuti Y. and Nasuti A.; 2018: *NTilt as an improved enhanced tilt derivative filter for edge detection of potential field anomalies*. *Geophys. J. Int.*, 214, 36-45.
- Nasuti Y., Nasuti A. and Moghadas D.; 2019: *STA: a novel approach for enhancing and edge detection of potential field data*. *Pure Appl. Geophys.*, 176, 827-841.
- Oksum E., Le D.V., Vu M.D., Nguyen T.H.T. and Pham L.T.; 2021: *A novel approach based on the fast-sigmoid function for interpretation of potential field data*. *Bull. Geophys. Oceanogr.*, 62, 543-556.
- Pham L.T., Oksum E. and Do T.D.; 2019: *Edge enhancement of potential field data using the logistic function and the total horizontal gradient*. *Acta Geod. Geophys.*, 54, 143-155.
- Pham L.T., Oksum E., Le D.V., Ferreira F.J.F. and Le S.T.; 2021: *Edge detection of potential field sources using the soft sign function*. *Geocarto Int.*, 37, 4255-4268, doi: 10.1080/10106049.2021.1882007.
- Pickering S.M. and Murray J.B.; 1976: *Geologic map of Georgia*. Georgia Geologic Survey, Georgia Department of Natural Resources, Geologic and Water Resources Division, Atlanta, GA, USA, scale 1:500,000.
- Prasad K.N.D., Pham L.T. and Singh A.P.; 2022: *Structural mapping of potential field sources using BHG filter*. *Geocarto Int.*, 37, 11253-11280, doi: 10.1080/10106049.2022.2048903.
- Reid A.B., Fitzgerald D. and Flanagan G.; 2005: *Hybrid Euler magnetic basement depth estimation: Bishop 3D tests*. In: *Expanded Abstracts, 75th Annual International Meeting, Society of Exploration Geophysicists, Houston, TX, USA*, pp. 671-673.
- Roest W.R.J., Verhoef J. and Pilkington M.; 1992: *Magnetic interpretation using the 3-D analytic signal*. *Geophys.*, 57, 116-125.
- Shahba S., Arjmandi R., Monavari M. and Ghodusi J.; 2017: *Application of multi-attribute decision-making methods in SWOT analysis of mine waste management (case study: Sirjan's Golgohar iron mine, Iran)*. *Resour. Policy*, 51, 67-76.
- Sun Y., Yang W., Zeng X. and Zhang Z.; 2016: *Edge enhancement of potential field data using spectral moments*. *Geophys.*, 81, G1-G11.
- Weiherrmann J.D., Ferreira F.J.F., Oliveira S.P., Cury L.F. and de Souza J.; 2018: *Magnetic interpretation of the Paranaquá Terrane, southern Brazil by signum transform*. *J. Appl. Geophys.*, 154, 116-127.
- Wijns C., Perez C. and Kowalczyk P.; 2005: *Theta map: edge detection in magnetic data*. *Geophys.*, 70, L39-L43.
- Williams S.E., Fairhead J.D. and Flanagan G.; 2005: *Comparison of grid Euler deconvolution with and without 2D constraints using a realistic 3D magnetic basement model*. *Geophys.*, 70, L13-L21.
- Winsor C.P.; 1932: *The Gompertz curve as a growth curve*. *PNAS*, 18, 1-8, doi: 10.1073/pnas.18.1.1.

Corresponding author: Ahmad Alvandi
 Institute of Geophysics, University of Tehran
 North Kargar Ave., Tehran, Iran
 Phone: +98 216 111 3411; e-mail: aalavndi@ut.ac.ir